12. A. J. Miller *et al.*, *Geophys. Res. Lett.* **19**, 929 (1992).
13. We computed stratospheric O_3 changes by first taking Total Ozone Measurement Satellite (*28*) trends for each 10° latitude band between 65°N and 65°S over the period 1979 to 1989 for each month. Poleward of 65°N and 65°S, the values at 65°N and 65°S were used. We converted the trends in total O_3 to trends in O_3 at each model level by assuming a constant percentage loss in the 7 km immediately above the tropopause (*3*). For the two model layers above this, we used a percentage loss rate of half that used in the lower layers. The position of the tropopause was defined from observed climatological average values. We computed the O_3 values by multiplying the trends by the number of years since 1974 and adding the result to the unperturbed values in (*11*).
14. The radiosonde data set is based on operationally received monthly averages, data from publications, data requested from national sources, and, for the South Pole, from the Comprehensive Aerological Reference Data Set (*29*). Data are for standard levels (850, 700, 500, 300, 200, 150, 100, and 50 hPa). Gross error and hydrostatic checks were applied (*30*). Comparisons with colocated Microwave Sounding Unit data since 1979 were used to assess and remove biases associated with recent instrumental changes at radiosonde stations operated by Australia and at some New Zealand stations. This reduced the cooling at 50 hPa since 1980 by about 2°C at some stations, with a noticeable impact on the Southern Hemisphere subtropical zonal average changes. The station data were gridded on a 5° latitude by 10° longitude grid as monthly anomalies (with respect to 1971 through 1990). Missing gridboxes were filled with the average of the anomalies in neighboring gridboxes, if at least three of these, out of a maximum of eight, had data. Unlike (*31*), no spatial interpolation was done. We converted the "filled" gridded data set to zonal monthly mean anomalies for each 10° latitude band at each pressure level by averaging with the requirement that there be at least 4 out of 36 longitude points present. If this was not the case, then for that latitude the zonal mean value was set to missing data. We converted the monthly average zonal mean anomalies to annual mean anomalies by averaging the 12 monthly values. At each latitude-pressure point, there must be at least 8 months with data; otherwise, the point was set to missing data in the annual mean.
15. K. P. Shine, Y. Fouquart, V. Ramaswamy, S. Solomon, J. Srinivasan, *Climate Change 1995: The Science of Climate Change* (Cambridge Univ. Press, Cambridge, 1996), pp. 108–118.
16. Over the period 1961 to 1995, in the HADCM2 simulations, the global mean forcing due to greenhouse gases increases by 1.5 W/m^2, whereas the negative global mean forcing due to tropospheric sulfate aerosols decreases by 0.23 W/m^2.
17. The pattern correlation (*R*) and the congruence (*g*) statistics are defined according to the following expressions:

$$R = \frac{\sum_{i,j} (M_{i,j} - \bar{M})(O_{i,j} - \bar{O})W_{i,j}}{\sqrt{\sum_{i,j} (M_{i,j} - \bar{M})^2 W_{i,j} \sum_{i,j} (O_{i,j} - \bar{O})^2 W_{i,j}}}$$

and

$$g = \frac{\sum_{i,j} M_{i,j} O_{i,j} W_{i,j}}{\sqrt{\sum_{i,j} M_{i,j}^2 W_{i,j} \sum_{i,j} O_{i,j}^2 W_{i,j}}}$$

where *i* and *j* are indices over latitude and pressure, $M_{i,j}$ is the model signal, $O_{i,j}$ designates the observed values, and $W_{i,j}$ is a weighting field. The spatial average, $\bar{F}$, for the model ($\bar{M}$) and the observations ($\bar{O}$) is

$$\sum_{i,j} F_{i,j} W_{i,j} \Big/ \sum_{i,j} W_{i,j}$$

Where, in either field, a data point was missing, that point was not included in the above computations. The weight arrays used are

$$\text{mass: } W_{i,j} = \cos \theta_i \tfrac{1}{2} (P_{j+1} - P_j)$$

$$\text{volume: } W_{i,j} = \cos \theta_i \tfrac{1}{2} (\log P_{j+1} - \log P_j)$$

where θ_i is the latitude and P_j is the pressure.
18. D. J. Karoly *et al.*, *Clim. Dyn.* **10**, 97 (1994).
19. B. D. Santer *et al.*, *ibid.* **12**, 77 (1995).
20. B. D. Santer, T. M. L. Wigley, P. D. Jones, *ibid.* **8**, 265 (1993).
21. Segments of zonal mean atmospheric temperature 35 years long were taken from the control integration. The start year of each segment was offset from the start year of the previous segment by 5 years giving a total of 129 segments. For each segment, means for years 1 to 20 (corresponding to 1961 through 1980 of the observations and forced simulations) and for years 26 to 35 (corresponding to 1986 through 1995 of the observations and forced simulations) were computed and differenced.
22. The *R* and *g* statistics computed between the control and forced signals have an estimated 70 to 80 degrees of freedom (*32*). Thus, a conservative estimate of the significance level of statistics greater than the maximum control value is 2%.
23. B. Efron and R. J. Tibshirani, *An Introduction to the Bootstrap* (vol. 57 of Monographs on Statistics and Applied Probability, Chapman and Hall, New York, 1993).
24. W. H. Press, S. A. Teukolsky, W. T. Vetterling, B. P. Flannery, *Numerical Recipes in Fortran: The Art of Scientific Computing* (Cambridge Univ. Press, Cambridge, ed. 2, 1992).
25. For each of the four forced signals and four statistics, we generated a probability distribution function (PDF) by (i) perturbing both forced simulations and observations by adding randomly selected segments of the control; (ii) computing trend patterns and four-member ensemble averages as before; (iii) computing *R* and *g* statistics between perturbed patterns; and (iv) repeating 2500 times to build a PDF. The resulting PDFs of *R* and *g* are non-Gaussian and biased with respect to the unperturbed values due to the normalization. This can be understood if one considers two patterns (P_1, P_2) that are perfectly correlated ($R = 1$). Adding noise to P_1 will reduce the correlation to less than 1. We correct with a Fisher *z* transformation (*24*), translating the transformed PDFs such that their average values are equal to the transformed values obtained with the unperturbed signals. Results in Table 2 are then computed directly from these transformed PDFs. We believe that the bias correction gives the most accurate risk estimates. Use of it does not affect our key result that SENS1 is, on balance, in best agreement with the observations.
26. G. Keating, D. Young, M. Pitts, *Adv. Space. Res.* **7**, 105 (1987).
27. D. Heath, P. K. Bhartia, R. D. McPeters, *J. Geophys. Res.* **89**(D4), 5199 (1984).
28. *Tech. Rep. 37* (Word Meteorological Organization, Geneva, 1994).
29. R. E. Eskridge *et al.*, *Bull. Am. Meteorol. Soc.* **76**, 1759 (1995).
30. D. E. Parker and D. I. Cox, *Int. J. Climatol.* **15**, 473 (1995).
31. A. H. Oort and H. Liu, *J. Climate* **6**, 292 (1993).
32. F. W. Zwiers and H. von Storch, *ibid.* **8**, 336 (1995).
33. T. Johns carried out the G and GS ensemble simulations. D. Sexton and D. Karoly produced the O_3 data set, using data provided by K. Shine. M. Gordon, D. Cullum, and M. O'Donnell carried out much of the processing required to produce the radiosonde data set. The work was partially supported by the U.K. Department of the Environment under contract PECD 7/12/37 (S.F.B.T., J.F.B.M., D.E.P., and computer time) and the U.K. Natural Environment Research Council and Wolfson College, Oxford (M.R.A.).

5 June 1996; accepted 26 September 1996

Dynamics of Oxidation of a Fe^{2+}-Bearing Aluminosilicate (Basaltic) Melt

Reid F. Cooper,* John B. Fanselow, J. K. Richard Weber†, Dennis R. Merkley, David B. Poker

Rutherford backscattering spectroscopy (RBS) and microscopy demonstrate that the ~1400°C oxidation of levitated droplets of a natural Fe^{2+}-bearing aluminosilicate (basalt) melt occurs by chemical diffusion of Fe^{2+} and Ca^{2+} to the free surface of the droplet; internal oxidation of the melt results from the required counterflux of electron holes. Diffusion of an oxygen species is not required. Oxidation causes the droplets to go subsolidus; magnetite (Fe_3O_4) forms at the oxidation-solidification front with a morphology suggestive of a Liesegang-band nucleation process.

The structure and dynamics of silicate melts are first-order dependent on the valence state of incorporated transition metal cations, particularly, in the case of geological melts, iron (*1*, *2*). As a consequence, understanding the chemical diffusion process by which a melt comes into redox equilibrium with its environment is critical in characterizing its structural and chemical evolution. Diffusion studies have emphasized two approaches: (i) oxygen (^{18}O) tracer diffusion experiments [for example, (*3*, *4*)] and (ii) transition-metal-cation redox experiments, which are analyzed based on the assumption that diffusion of an oxygen species dominates the redox kinetics [for example, (*5*–*7*)]. There is a noted discrepancy between the

---

R. F. Cooper and J. B. Fanselow, Departments of Materials Science and Engineering and Geology and Geophysics, University of Wisconsin–Madison, 1500 Engineering Drive, Madison, WI 53706, USA.
J. K. R. Weber and D. R. Merkley, Intersonics Incorporated, 3453 Commercial Avenue, Northbrook, IL 60062, USA.
D. B. Poker, Oak Ridge National Laboratory, Mail Stop 6048, Post Office Box 2008, Oak Ridge, TN 37831, USA.

*To whom correspondence should be addressed.

†Present address: Containerless Research, Inc., 910 University Place, Evanston, IL 60201, USA.

results of the two types of experiments: for similarly polymerized melts, the ^{18}O tracer diffusion coefficient is found to be 10^1 to 10^3 times smaller than the diffusion coefficient determined in the redox experiments (8). This discrepancy has been attributed to different mechanisms of oxygen transport for the two types of experiments: the slower tracer diffusion is ascribed to the motion of molecular O_2 or of poly-anionic complexes, whereas the redox reactions might occur by way of ionic diffusion of the smaller O^{2-} [for example, (*5*, *7*)].

An iron-bearing aluminosilicate melt is a polaron-type semiconductor (9), however, and thus the dissipation of a redox potential need not involve motion of an oxygen species at all: a more rapid, parallel kinetic response could instead involve the charge-coupled motion of fast moving network-modifying cations and faster moving electronic species (electrons or holes) (*10*). Such a response is noted, for example, in the oxidation of ferromagnesian olivine, in which the most rapid dissipation of the oxidation potential occurs by the chemical diffusion of Mg^{2+} and Fe^{2+} to the free surface (through a vacancy mechanism), charge-compensated by a counterflux of holes. The result is a characteristic, metastable reaction morphology that includes the formation of a ferrite surface film and the internal precipitation of Fe_3O_4 and amorphous SiO_2 within an iron-free Mg_2SiO_4 matrix (*11*). Could such a mechanism be operative in the redox dynamics of iron-bearing silicate melts and so explain the discrepancy in the diffusion behavior noted above? There is some indirect evidence that such is the case: the melt redox experiments described above show chemical diffusion rates that compare well with the tracer diffusivity of divalent cations (*3*, *8*, *12*).

We report here on a set of experiments to evaluate qualitatively the mechanism of oxidation of a basaltic melt. We use RBS to examine chemical change at and near the free surface of the melt: a build-up of network modifying cations at the surface, and evidence of their depletion below the surface, is diagnostic of the cation diffusion mechanism (*10*, *13*). Because there exist other ways to extract cations from silicates [for example, having the specimen in contact with (or in line-of-sight of) platinum causes notable extraction of Fe (*14*)], we used aeroacoustic levitation (AAL), a containerless technique in which a melt droplet is levitated on a gas jet, positioned and stabilized with acoustic waves, and heated with a laser [see (*15*)]. The specimen therefore has contact only with the levitating gas.

Specimens were originally glass, prepared by the melting and quenching of a nepheline-normative olivine basalt from the Columbia River plateau (*16*). Specimens were hand-ground to an average diameter of 3 mm. Specimens were levitated with a preheated (250°C) gas jet of either high-purity argon [oxygen activity (partial pressure) of $p_{O_2} \approx 5 \times 10^{-6}$] or dry, bottled air ($p_{O_2}$ = 0.21). Droplet heating involved a split CO_2 laser beam illuminating the specimen on opposite sides to promote uniform heating; temperature was measured and controlled (CCD feedback) with two optical pyrometers. Specimens were initially melted for a duration of ~30 s at a temperature (*T*) of ~1400°C while levitated on the Ar jet. These (*T*, p_{O_2}) conditions were slightly oxidizing: the fayalite-magnetite-quartz (FMQ) oxygen buffer at 1400°C is $p_{O_2} \approx 5 \times 10^{-7}$ (*17*). The quenched droplets were again levitated and melted on air at ~1400°C for ~5 s. The droplets formed in gas-jet levitation have flattened bottoms.

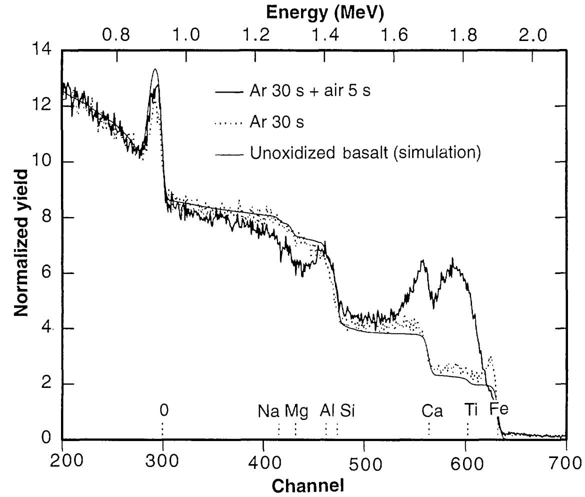

Fig. 1. Rutherford backscattering spectroscopy spectra from the bottom of basalt melt droplets following levitation-melting-quench cycles. The spectra shown are compared to the simulated spectrum for the unoxidized material (*19*). The elemental labels on the energy-channel scale represent the energy of backscattered α particles upon encountering a nucleus of the labeled atom on the surface of the specimen. Examination of the simulation for the unoxidized basalt (fine solid line) indicates that all species are present at the surface and the composition is uniform with depth (the uniformity is easily seen as the nearly flat yields behind the Ca and Na energy "edges"). (The peak seen at the edge for oxygen is a non-Rutherford resonance resulting from the use of 2.5 MeV α particles.) Oxidation conditions of 1400°C, with Ar, for 30s (dotted spectrum) causes a peak in the backscattered yield for Fe at the specimen surface; the source of this iron is at depth in the droplet, as evidenced by the drop in backscattering yield between 1.4 and 1.3 MeV. The addition of 1400°C with air for 5 s oxidation (heavy-line spectrum) results in a substantial amount of iron oxide on the surface, as well as some calcium oxide. The Si edge, still at the backscattered energy characteristic of its surface presence, is notably lowered in yield: partial coverage of the surface by Ca and Fe oxides is thus indicated. Again, the source of Fe and Ca now at the surface is from depth in the specimen, indicated by the drop in backscattering yield below 1.4 MeV.

After levitation in Ar, the quenched droplets had a black, specular (metallic) luster, notably different from the vitreous surface finish of the starting basaltic glass. Upon the second levitation in air, the bottom surface (that is, the surface in contact with the levitation gas) developed a specular finish with bright brown-to-blue coloration, and fine (≤1 μm) crystallites formed there. The remainder of the droplet retained the black specular finish.

Rutherford backscattering spectroscopy spectra (18) reveal that the reaction morphology was associated with cation diffusion-dominated oxidation kinetics. In Fig. 1, the spectra from the bottoms of droplets levitated in Ar and Ar + air are compared with a spectral simulation for the original (unoxidized) basalt glass (*19*). Levitation melting in Ar produced a distinct peak in the spectrum at the characteristic energy for encountering Fe at the free surface and a loss of overall backscattering yield at finite depth (energy of 1.4 to 1.3 MeV). Furthermore, the Si energy edge became slightly tilted. This spectral signature indicates that the small oxidation potential created a thin, discontinuous surface film of iron oxide on top of a silicate composition depleted in iron. Although the surface iron oxide film is thin, it is sufficient to produce the black specular luster on the quenched droplet.

The effect of the 5-s air levitation on the RBS spectrum is dramatic: a large peak for Fe appeared at the specimen surface, although its maximum value was slightly below the surface. Calcium, too, was concentrated at the surface (the Ca edge is only slightly larger than its original size; the apparently large Ca peak in the spectrum is primarily a result of the Ca yield lying on top of that for Fe). The source at depth of the Fe and Ca on the surface is easily evident in the lowering of backscattering yield for energies below ~1.4 MeV. Silicon remains at the free surface but at a lower concentration. The effects of oxidation on Na and Mg as a result of the oxidation cannot be resolved. The RBS spectrum from the top of an air-oxidized droplet, however, is little different from that seen for the bottom of an Ar-only levitated droplet.

Microscopic observations of air-oxidized droplets (Fig. 2) revealed two distinct internal reaction fronts, points ξ''' and ξ''. Point ξ''' is an oxidation-crystallization front (Fig. 2, B and C). As shown by transmission electron microscopy, the crystalline phase between the two fronts is magnetite (Fe_3O_4); hematite (α-Fe_2O_3) and pseudo-wollastonite (β-$CaSiO_3$) are present below ξ''. Iron has been extracted from the melt at the oxidation front (Fig 2B): the tan color has been lost, in bands, immediately above ξ'''. Color is returned in the region containing hematite (between the droplet bottom surface and ξ'': dark brown in Fig. 2B; a lighter reddish brown in Fig. 2D).

The presence of hematite between the near-surface and reaction front ξ'' indicates that the reaction temperature near the bottom of the droplet could not have exceeded ~1380°C; above this temperature magnetite, and not hematite, is the stable form of iron oxide in air (*20*). The greater extent (depth) of the overall reaction near the center (vertical axis) of the droplet indicates that the droplet interior was warmer than the exterior, which was cooled by the levitation gas jet. The concentration of the reaction where the levitation gas jet impinged on the specimen, and the relative lack of reaction on the sides and top of the droplet confirm that flow of the jet was laminar: a low-pressure, low-p_{O_2} wake envelope was produced immediately downstream (that is, beyond the horizontal center plane) of the droplet. The color removal in bands at the oxidation front ξ''' is clearly suggestive of a Liesegang-band-type nucleation process for the magnetite (*21*); the phenomenon occurred for two reasons: the extraction of iron from the melt affected both the transport rate of electronic defects (via the drop in concentration) as well as decreased the local concentration of Fe^{3+} in the glass such that the thermodynamic barrier to nucleation cannot be satisfied until additional Fe diffuses to ξ''' from depth.

Our quantitative studies of oxidation dynamics in Fe^{2+}-bearing aluminosilicate glasses (*8*, *19*) and these data imply that the oxidation process in the levitated basalt melt can be described as an isothermal undercooling phenomenon. Temperatures of 1350° to 1400°C are above the liquidus for the Fe^{2+}-bearing composition we used. Oxidation caused a shift of the liquidus such that magnetite nucleated (*2*) (Fig. 3). The physics involves the chemical diffusion of divalent cations to the free surface, the fluxes of which are charge-compensated by a counterflux of rapidly mobile electron holes (*22*). Internal nucleation of magnetite at ξ''', transformation of magnetite to hematite at ξ'', and the growth of Ca-Fe oxides at the free surface ($\xi = 0$), as diffusing cations react with environmental oxygen, results. The growth of each layer (that is, the relative motions of ξ', ξ'', and ξ''') is proportional to the square root of elapsed time as the chemical potential for oxygen is fixed at each labeled location. For each 2 moles of electron holes reaching ξ''', 1 mole of magnetite is formed, 1 mole of divalent cations is released to diffuse to the free surface, and the residual melt is almost entirely depleted of iron; as a consequence, each mole of magnetite formed represents many moles of melt reacted (on the order 10) and so the depth to ξ''' grows much faster than does the layer of surface oxides. Divalent cation diffusion from $\xi = \xi'''$ to $\xi = 0$ thus becomes rate-limiting for the reaction. Another ramification of the iron depletion from the melt at ξ''' is the chemical potential created for divalent cation interdiffusion beyond ξ''': this interdiffusion contributes to the apparent formation of Liesegang bands. The formation of pseudowollastonite between ξ'' and $\xi = 0$ most likely occured during the rapid cooling of the droplet, suggesting that hematite is a more efficient substrate for heterogeneous nucleation of pyroxene than is the ferrite.

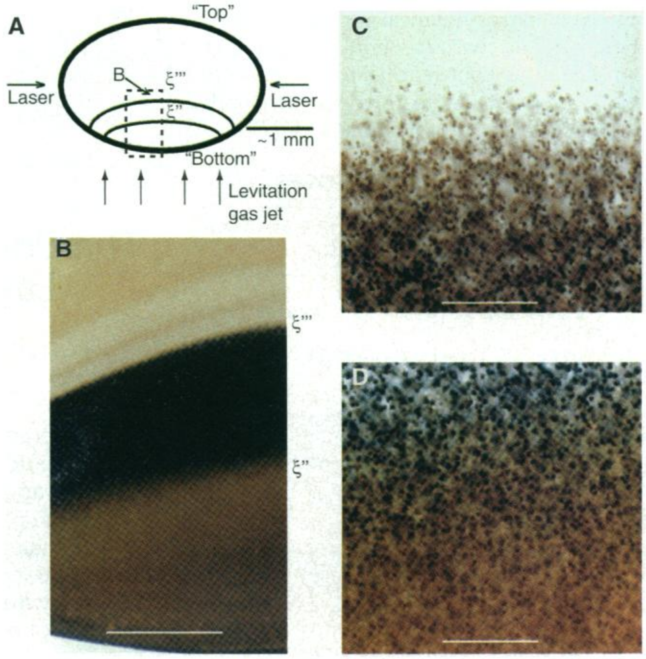

Fig. 2. Microstructure of basalt droplet after levitation-melting-quench cycles at 1400°C in Ar for 30 s plus at 1400°C in air for 5 s. **(A)** Cross-sectional schematic of the levitated, oxidized and quenched droplet. Two internal reactions fronts, ξ'' and ξ''', are identified in the droplet. **(B)** Transmitted optical micrograph of the droplet region noted in (A). The extraction of color in bands beyond ξ''' suggests that a Liesegang nucleation process is operative at the oxidation-crystallization front (scale bar: 250 μm). **(C)** Detail at reaction front ξ'''. The opaque phase, seen here having cubic symmetry, was identified by electron diffraction as magnetite (Fe_3O_4) (scale bar: 25 μm). **(D)** Detail at reaction front ξ''. The loss of opaque magnetite is evident. Electron diffraction in this region identified two crystalline phases, hematite (α-Fe_2O_3) and pseudowollastonite (β-$CaSiO_3$) (scale bar: 25 μm).

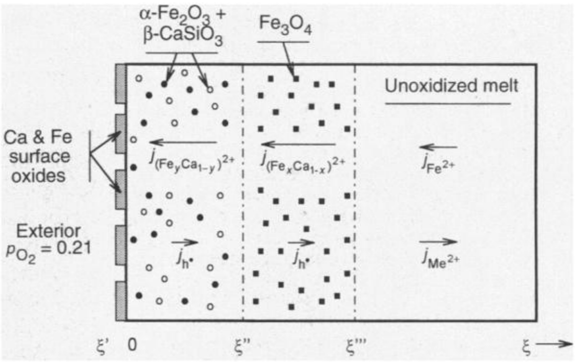

Fig. 3. Oxidation dynamics in the molten basalt at ~1400°C, consistent with the RBS and microstructural evidence. Oxidation involves chemical reactions at two internal fronts and at the free surface of the droplet, as well as chemical diffusion through the product, oxidized and nucleated partial melt. (Variable *j* denotes diffusive flux, with the subscript denoting the species.) At the internal oxidation-crystallization front ξ''', in-fluxing electron holes ($h^\bullet$) react with the unoxidized melt to produce magnetite (the liquidus reaction for the oxidized material) and to release Fe^{2+} and Ca^{2+} ions to diffuse to the free surface. These divalent cations subsequently react with environmental oxygen to produce surface oxide phases that partially cover the free surface. The surface reaction also produces the $h^\bullet$ for inward diffusion. Because the mobility of divalent cations is much lower than that of the $h^\bullet$, oxidation is rate-limited by cation diffusion. The formation of magnetite extracts most (but not all) of the Fe^{2+} from the melt, creating the interdiffusion potential for Fe^{2+} and other divalent species (Me^{2+}) in the otherwise unreacted melt beyond ξ'''; one result is the apparent formation of Liesegang nucleation bands at the front. Mass balance considerations require that the depth to ξ''' be more than an order-of-magnitude greater than the average thickness of the discontinuous Fe and Ca oxides that form on the free surface. The second internal reaction front, ξ'', sees the magnetite oxidized to hematite. Because of the amount of Fe extracted from the melt to produce the original magnetite, the second oxidation requires a greater contribution of outward flux from Ca^{2+} (*x* has a magnitude close to unity while *y* is near zero).

These results demonstrate that redox chemical diffusion experiments do not a priori allow characterization of the diffusion coefficient of an oxygen species in a Fe-bearing aluminosilicate melt. Differences in values of diffusion coefficients extracted from a redox experiment and an oxygen tracer diffusion experiment on the same melt composition would therefore reflect that the two procedures are measuring different things. Our experiments additionally demonstrate that the cation-diffusion response to a redox driving force allows for relatively rapid chemical segregation in a melt; the mechanism should perhaps be considered as contributing to the concentric segregation microstructures frequently described for primitive chondrules (*23*).

REFERENCES AND NOTES

1. P. C. Hess, *Origins of Igneous Rocks* (Harvard Univ. Press, Cambridge, MA, 1989), chap. 5.
2. P. L. Roeder and E. F. Osborn, *Am. J. Sci.* **264**, 428 (1966).
3. T. Dunn, *Geochim. Cosmochim. Acta* **46**, 2293 (1982).
4. D. Canil and K. Muehlenbachs, *ibid.* **54**, 2947 (1990).
5. T. Dunn, *ibid.* **47**, 1923 (1983).
6. H. D. Schreiber, S. J. Kozak, A. L. Fritchman, D. S. Goldman, H. A. Schaeffer, *Phys. Chem. Glasses* **27**, 152 (1986).
7. R. F. Wendlandt, *Contrib. Mineral. Petrol.* **108**, 463 (1991).
8. G. B. Cook, R. F. Cooper, T. Wu, *J. Non-Crys. Solids* **120**, 207 (1990).
9. J. Zarzycki, *Glasses and the Vitreous State* (Cambridge Univ. Press, Cambridge, UK, 1991), chap. 11.
10. H. Schmalzried, *Solid State Reactions* (Verlag Chemie, Weinheim, Federal Republic of Germany, ed. 2, 1981), chap. 8.
11. T. Wu and D. L. Kohlstedt, *J. Am. Ceram. Soc.* **71**, 540 (1988); D. L. Kohlstedt, C. Goetze, W. B. Durham, J. VanderSande, *Science* **191**, 1045 (1976).
12. E. B. Watson, *Earth Planet. Sci. Lett.* **52**, 291 (1981).
13. H. Schmalzried, *Ber. Bunsenges. Phys. Chem.* **87**, 551 (1983).
14. T. L. Grove, *Contrib. Mineral. Petrol.* **78**, 298 (1981); D. L. Kohlstedt and S. J. Mackwell, *ibid.* **95**, 226 (1987).
15. J. K. R. Weber *et al.*, *Rev. Sci. Instrum.* **65**, 456 (1994). Basalt droplet levitation required a gas flow rate of ~3 l min^{-1} (jet velocity of ~18 m s^{-1}). Heating a droplet to 1400°C, by focusing the laser, took 5 to 7 s; quenching occurred more rapidly. At the 1400°C processing temperature, the actual temperature across the droplet varied by ~50°C; the bottom of the droplet was cooler than the sides.
16. The composition (oxide weight percent) of the starting material is SiO_2, 43.7; TiO_2, 2.7; Al_2O_3, 14.3; FeO,12.2; MnO, 0.2; MgO, 9.5; CaO, 11.4; Na_2O, 3.3; K_2O, 1.1; P_2O_5, 0.7 (*19*). The glass was prepared by melting ~10 g of finely powdered rock in a high-purity Al_2O_3 crucible at 1450°C for 30 min at $p_{O_2} = 10^{-8}$. The melt was quenched within the controlled environment. Any glass contaminated with excess alumina, as determined by electron-probe spectroscopy, was ground away. The resultant glass, black in color, was chemically homogeneous and displayed no crystallization to the resolution of conventional optical microscopy.
17. J. Myers and H. P. Eugster, *Contrib. Mineral. Petrol.* **82**, 75 (1983).
18. 2.5 MeV α-particles ($^4He^{2+}$) were employed. Backscattering spectra were analyzed by an iterative simulation process [L. R. Doolittle, *Nucl. Instrum. Methods Phys. Res.* **B9**, 344 (1985)], which is based on the well-established database of ion-stopping and ion-backscattering cross sections [for example, J. F. Ziegler, J. P. Biersack, U. Littmark, *The Stopping and Range of Ions in Solids* (Pergamon, New York, 1985)]. The α-particle beam has a spot diameter of ~1 mm; the flattened bottoms of quenched droplets could be easily and directly analyzed. The beam spans an arc of ~12° on the tops of droplets; this produces an error in backscattering yield of ~10%, for which a correction is accomplished in the simulation analysis.
19. R. F. Cooper, J. B. Fanselow, D. B. Poker, *Geochim. Cosmochim. Acta* **60**, 3253 (1996).
20. A. Muan and E. F. Osborn, *Phase Equilibria Among Oxides in Steelmaking* (Addison-Wesley, Reading, MA, 1965).
21. C. Wagner, *J. Colloid Sci.* **5**, 85 (1950); D. L. Ricoult and H. Schmalzried, *Ber. Bunsenges. Phys. Chem.* **90**, 135 (1986).
22. The gradient in oxygen chemical potential in the residual oxidized melt is physically manifest by a gradient in the concentration of polarons (electron holes), which are distorted Fe^{3+} modifier–O^{2-} bonds; it is through these distortions, these "point defects," that modifier divalent cation diffusion occurs (*19*).
23. Some reduced, primitive chondrules, for example, in Semarkona (LL3), display concentric rings of internal metal precipitation [for example, J. T. Wasson, *Meteorites: Their Record of Early Solar System History* (Freeman, New York, 1985), chap. 7]. Such a microstructure is characteristic of a dynamic reduction process for the liquid that is a mirror-image of oxidation, that is, oxygen is ablated at the surface, divalent cations diffuse inward while electron holes counter-diffuse toward the surface; iron precipitates at an internal reduction front [compare with, H. Schmalzried, *Ber. Bunsenges. Phys. Chem.* **88**, 1186 (1984)]. We have evidenced this reduction process in recent experiments on a synthetic basalt analog.

24. This work was funded, in part, by a grant (to R.F.C.) from the National Aeronautics and Space Administration, Division of Microgravity Sciences and Applications (NAGW-2835). Rutherford backscattering spectroscopy was performed at the Center for Surface Modification and Characterization at Oak Ridge National Laboratory, which is sponsored by the Division of Materials Sciences, U.S. Department of Energy (DE-AC05-96OR22464).

29 April 1996; accepted 7 October 1996

The Edge of Time: Dating Young Volcanic Ash Layers with the ^{40}Ar-^{39}Ar Laser Probe

Yanshao Chen, Patrick E. Smith, Norman M. Evensen, Derek York, Kenneth R. Lajoie

Argon-40–argon-39 single-crystal dating of young (5000 to 30,000 years ago) volcanic ash layers erupted from the Mono Craters, California, shows that the method can yield meaningful ages in Holocene tephra. Because of ubiquitous xenocrystic contamination, the data do not form isochrons but plot in wedge-shaped regions on an argon isotopic diagram. The upper boundary of the region is an isochron matching the ^{14}C-derived age of the eruption. Such contamination-related patterns may be common in dating young materials by the single-crystal method. Argon dating by this method can help refine the time scale of physical and biological evolution over the past 100,000 years.

Nature has endowed the potassium-argon geochronometer with great power. The 1.3-billion-year half-life of the parent, ^{40}K, allows the geochronometer to be used to date events back to the creation of the solar system, while the efficiency with which minerals typically exclude ambient argon at their formation makes it a sensitive tool for dating the recent past. The ^{40}Ar-^{39}Ar method of reading the K-Ar clock and the laser step-heating procedure for the analysis of single grains add to its versatility and resolution (*1*). Argon dating of the last 100,000 years, while technically difficult, can complement ^{14}C and other dating tools, and could be invaluable in resolving uncertainties and ambiguities in other methods.

Dating of sanidine crystals separated from rhyolitic lavas from the Mono Craters, California, demonstrated the feasibility of using ^{40}Ar-^{39}Ar single-crystal laser-probe analysis to date suitable material as young as 12.5 thousand years ago (ka) with approximately 5% precision (*3*). However that study did not rule out the possible presence of excess radiogenic ^{40}Ar (*4*) at a uniform concentration in the sanidine crystals, corresponding to a quantum of erroneous excess age, because no independent measurement of the eruptive age was available. We have therefore analyzed sanidine crystals from three tephra layers, also in the Mono Craters area, for which ^{14}C age control exists.

The Mono Craters, a string of volcanic domes, flows, and explosion craters in central California, erupted episodically in the late Quaternary, depositing layers of ash in adjacent Mono Lake and in nearby meadows. We analyzed two ash layers (WCA-8 and WCA-15) in the late Pleistocene Wilson Creek Formation (WCF), a lacustrine silt deposited during the last deep-water phase of Mono Lake (*5*). We also dated an ash layer (CMA-13) in a sequence of Holocene peat deposits in Crooked Meadow, directly southeast of Mono basin (*6*). Inter-

---

Y. Chen, P. E. Smith, N. M. Evensen, D. York, Department of Physics, University of Toronto, 60 Saint George Street, Toronto, Ontario M5S 1A7, Canada.

K. R. Lajoie, U.S. Geological Survey, 345 Middlefield Road, MS-977, Menlo Park, CA 94025–3591 USA.